buildings

MDPI

Article

Georadar Survey and Simulation for Subsurface Investigation at Historical Mosque of Sorghatmesh, Cairo, Egypt

Mohamed Elkarmoty [1,2], Hussien E. Allam [2,3,*], Khalid Helal [1,2], Fathy Ahmed [2,4], Stefano Bonduà [5] and Sherif A. Mourad [2,6]

1 Department of Mining, Petroleum, and Metallurgical Engineering, Faculty of Engineering, Cairo University, 1 Gamaa Street, Giza 12613, Egypt; mohamed.elkarmoty@cu.edu.eg (M.E.); eng_khalidezz@cu.edu.eg (K.H.)
2 UNESCO Chair on Science and Technology for Cultural Heritage, Faculty of Engineering, Cairo University, 1 Gamaa Street, Giza 12613, Egypt; eng.fathyahmed25@gmail.com (F.A.); smourad@eng.cu.edu.eg (S.A.M.)
3 Rock Engineering Laboratory, Faculty of Engineering, Cairo University, 1 Gamaa Street, Giza 12613, Egypt
4 Engineering Center for Archaeology and Environment, Faculty of Engineering, Cairo University, 1 Gamaa Street, Giza 12613, Egypt
5 Department of Civil, Chemical, Environmental and Materials Engineering, University of Bologna, Via Terracini 28, 40131 Bologna, Italy; stefano.bondua@unibo.it
6 Department of Structural Engineering, Faculty of Engineering, Cairo University, 1 Gamaa Street, Giza 12613, Egypt
* Correspondence: hussienessamgeoph@gmail.com

Abstract: Sorghatmesh mosque is a historical structure that was constructed in Cairo, Egypt, by Prince Saif El-Din Sorghatmesh in 1356. A dual-frequency ground-penetrating radar (GPR) with 250–700 MHz was used to investigate the subsurface of the Sorghatmesh mosque for restoration purposes. A total of 37 lines were surveyed on the ground floor of the mosque. The subsurface utilities were detected, and the status of the concrete base and the medium of the ground floor were assessed. A set of subsurface anomalies were detected and interpreted within the ground floor area of the mosque. In order to validate the interpretation, a trial pit was drilled on the ground floor, allowing for the visual inspection of the subsurface, and a Georadar numerical simulation was carried out to study the responses of the subsurface materials and conditions. For a better comprehension of the results, the ground floor area was categorized into five zones where the GPR interpretations between survey lines are almost similar. This work not only demonstrates the effectiveness of GPR as a non-invasive investigation tool but also highlights the potential of integrating advanced technologies into cultural heritage preservation by offering refined methodologies and insights for future research and restoration efforts.

Keywords: dual-frequency GPR; GPR simulation; subsurface assessment; cultural heritage; groundwater; subsurface utilities

check for updates

Citation: Elkarmoty, M.; Allam, H.E.; Helal, K.; Ahmed, F.; Bonduà, S.; Mourad, S.A. Georadar Survey and Simulation for Subsurface Investigation at Historical Mosque of Sorghatmesh, Cairo, Egypt. *Buildings* **2024**, *14*, 3653. https://doi.org/10.3390/buildings14113653

Academic Editor: Emilia Vasanelli

Received: 10 October 2024
Revised: 4 November 2024
Accepted: 7 November 2024
Published: 17 November 2024

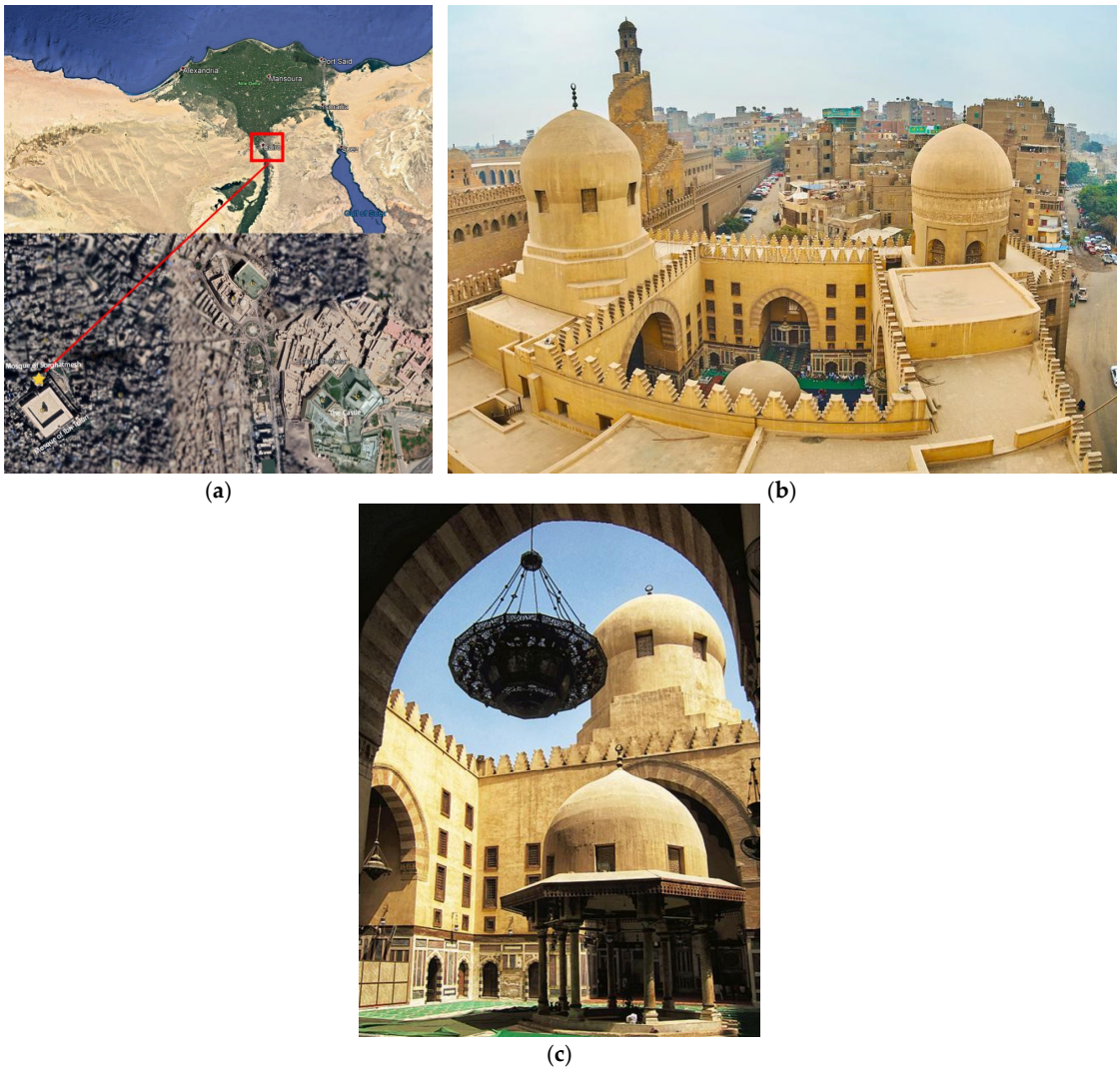
Copyright: © 2024 by the authors. Licensee MDPI, Basel, Switzerland. This article is an open access article distributed under the terms and conditions of the Creative Commons Attribution (CC BY) license (https://creativecommons.org/licenses/by/4.0/).

1. Introduction

The preservation of culture heritage sites represents a critical need and significant challenge, particularly in historically rich and culturally diverse countries like Egypt. Throughout history, Egypt was the main home for many great civilizations and empires including those of the ancient Egyptians, Ptolemaic, Roman, and Islamic. Some of these culture heritage sites have become damaged through time due to several factors. In order to maintain and restore these archaeological sites, a multidisciplinary approach is usually required, and the first step is documenting and evaluating the current statues of the monument based on non-destructive techniques (NDTs). In this study, Sorghatmesh mosque, an architectural masterpiece from the Islamic Era, faces structural challenges that threaten its integrity; therefore, restoration work was initiated to restore the monument.

In 1356, Prince Saif El-Din Sorghatmesh, one of the most powerful Mamluk's princes of Sultan Al-Nasir Badr al-Din Hassan ibn Muhammad ibn Qalawun (who was the sultan

of Egypt during two periods, 1347–1351 and 1354–1361), gave the order to construct a mosque [1–4]. Sorghatmesh mosque was built on El-Khedery Street in the old city of Al-Qata'I (current location is El-Saleba Street, in El-Sayda Zeinab district) on the western side of Ibn Tulun's mosque and near the Citadel of Cairo (Figure 1a). This mosque is regarded as one of the most beautiful mosques in Islamic Cairo, due to the use of various materials (wood, marble, and colored glass) in the decoration work and different styles (Geometrical shapes and different writing styles of Arabic words). It has four iwans; an iwan for each mazhb (way of Islamic thinking) was placed on the four internal sides of the mosque (Figure 1b). Its design was influenced by Persian architecture, and it is considered an example of the innovation of Mamluk's architecture (Figure 1c). The mosque's structure consists of three main parts: (i) the mosque; (ii) the school of teaching Islamic sciences; and (iii) the mausoleum of Prince Sorghatmesh [5–8]. This mosque and its school had a deep influence on the people of the Islamic world in those times; it was one of the very few places around the Islamic world in which Islamic sciences were being taught along with other sciences, like medicine and mathematics (the school was like university nowadays). Furthermore, the school hosted students from all around the world, and many great scientists from different fields gave lectures there, including the famous sociologist and historian Ibn Khaldun [1–4].



(**a**) (**b**)

(**c**)

Figure 1. (**a**) The location of Sorghatmesh mosque; (**b**) the outside architecture of the mosque with the presence of a unique spiral minaret architect; and (**c**) the inside structure of the mosque (open hall with a dome in the middle and 4 iwans facing each other).

The structure of the mosque suffered from the presence of several cracks, which indicate problems at the foundation of the mosque; although it has been repaired several times throughout its lifetime, none of these repairs were properly documented. The Egyptian authorities and the Ministry of Antiquities started a detailed investigation of the mosque in order to start the restoration work, given its unique and significant architecture and historical importance. One of the main tasks was performing non-destructive testing on this structure to evaluate potential risks and locate any defects (fractures, cracks, voids, groundwater rising) underneath the floor of Sorghatmesh mosque (which could have adverse effects if ignored) and provide engineering solutions for potential structural problems for the restoration work of the mosque. In order to non-destructively investigate the subsurface conditions of Sorghatmesh mosque, the ground-penetrating radar (GPR) technique was chosen to be the main investigation tool in this study.

Through the years, GPR has proven to be one of the best non-destructive investigation techniques for use in cultural heritage sites. GPR mainly depends on measuring and recording the response of GPR waves (electromagnetic (EM) pulses) after their transmission and reflection through the subsurface. These off-boundary reflections occur due to the different dielectric constants between the subsurface mediums [9]. After recording and processing these GPR data, radargram data must be interpreted in order to obtain a subsurface model representing all the structures or discontinuities underneath the area of study [10–17].

GPR was used for archaeological prospection and searching for hidden chambers adjacent to Tutankhamun's tomb in Luxor, Egypt, using three GPR systems with a wide range of frequencies (150–3000 MHz), and the study concluded that there was the absence of hidden voids behind the Tomb of Tutankhamun [18]. GPR was applied at the Collemaggio Basilica in Italy using medium and high frequencies to conduct non-invasive investigations for the restoration work of the historic building, and it was successful in detecting degrading spots and the thickness of walls [19]. GPR was also used at Tell Qubr Abu al-'Atiq in Syria to map the remains of a buried Early Bronze Age city; the study revealed the presence of uncovered streets, buildings, and walls of the city [20]. A GPR survey was conducted on the pavement of San Sebastiano's church in Catania, Sicily, to detect natural or anthropic buried cavities, and the GPR results revealed the presence of unknown subsurface structures [21]. GPR was also used to study the possible effects of the remodeling of the Roman Theatre of Sagunto (Valencia, Spain) on historical Roman remains based on the variation in GPR wave velocity [22]. GPR and Electrical Resistivity Tomography (ERT) surveys were performed to conduct a structural assessment of the Sarno Baths, Pompeii, and identify archaeological features; the study revealed the presence of high resistive anomalies by ERT, which were found to be lava deposits, and GPR detected a possible presence of archaeological remains and evaluated the structural elements of the monument [23]. An integrated assessment was carried out using ambient vibrations and Sonic and GPR measurements at The Rialto Bridge in Venice, Italy, to assess the structural integrity of the monument, in which GPR and UST proved to be useful in explaining the nature of the occurred damage based on the reduction in wave speed [24]. A joint interpretation of GPR, Terrestrial Laser Scanner (TLS) measurements, and chemical analyses was conducted to characterize a pre-Trajan wall structure in Rome, Italy; the study demonstrated the importance of using several non-destructive techniques to analyze archaeological structures [25]. A combination of non-destructive techniques including GPR, Infra-Red Thermography (IRT), and fiber-optics microscopy was implemented in the south upper gallery mosaic areas of Hagia Sophia, Turkey, to evaluate the preservation state of the zone; this used approach was successful in investigating the preservation state of the mosaic materials [26]. A case study of GPR, Terrestrial Light Detection and Ranging (T-LiDAR), and IRT Data fusion was performed to reconstruct the Roman Site "Aquis Querquennis" (Bande, Spain); this novel integration proved its effectiveness and allowed for the detection of several hidden constructions [27]. GPR was also used in many different applications related to cultural heritage sites [28–39].

The objective of this study is to evaluate the subsurface of Sorghatmesh mosque's floor using GPR as a non-destructive technique to assess the subsurface material conditions supporting GPR measurements with the aid of GPR numerical simulation to facilitate and support interpretation in contrast to the above-mentioned case studies. Furthermore, GPR numerical simulations were widely used in different applications to study the responses of GPR waves in different applications [40–48].

2. Site Characteristics

The location of Sorghatmesh mosque was very special in the time of construction, being near Ibn Tulun's mosque which was built on a high hill or mountain called Djabal Yashkur (the summit was about 50.0 m taller than the valley and was very steep towards the Nile valley). These specifications of the location were satisfying for Ibn Tulun's wish to build an indestructible mosque that could survive the Nile flooding. This limestone hill is geologically considered an extension of the Muqattam spur [49]. Nowadays, this hill elevation is only noticeable in Ibn Tulun's mosque, but the elevation of Sorghatmesh mosque is currently on the same ground level as the surrounding streets. The mosque consists of many floors with many available rooms which were used to host students from all around the world. This study focuses on the ground floor which may be subdivided into different parts (Figure 2). The central part is an open-air court surrounded by four iwans on each side of the hall; one of those iwans is currently used as a praying room (the iwan located southeast), with a dome located in the middle of this hall. The mausoleum is located on the ground floor also. There is an area of bathrooms, the rest of the floor consists of many rooms, and there is a separating area outside the mosque that separates it from Ibn Tulun's mosque.

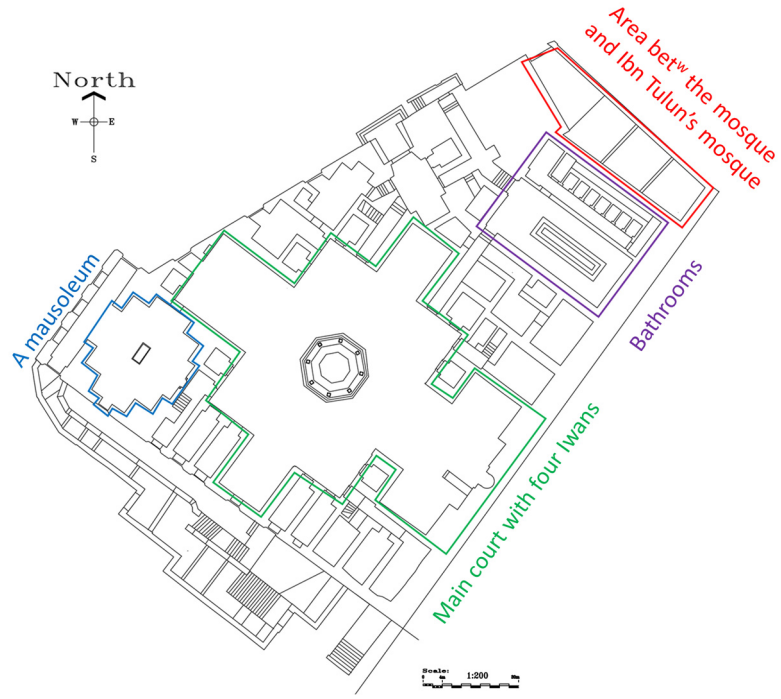


Figure 2. The ground floor structural plan of the mosque.

3. Georadar Survey

GPR devices mainly consists of transmitters (to transmit EM wave pulses), receivers (to receive the transmitted/reflected EM wave pulses), and control units to trigger, control, and record the EM wave pulses (as illustrated in Figure 3a). In this study, the GPR measurements were carried out on the ground floor of Sorghatmesh mosque using a dual-frequency GPR antenna (250–700 MHz) manufactured by IDS GeoRadar (Figure 3). This device has the

advantage of measuring GPR profiles using two frequencies: the high frequency (700 MHz) provides shallow penetration depth with high-resolution imaging, while the second frequency (250 MHz) provides deep penetration depth with lower-resolution imaging. This device produces two radargrams (for each antenna frequency) for the same GPR profile. The locations of the GPR profiles were distributed to cover all the available locations on the ground floor of the mosque and surveyed using the total station device (Figure 4).

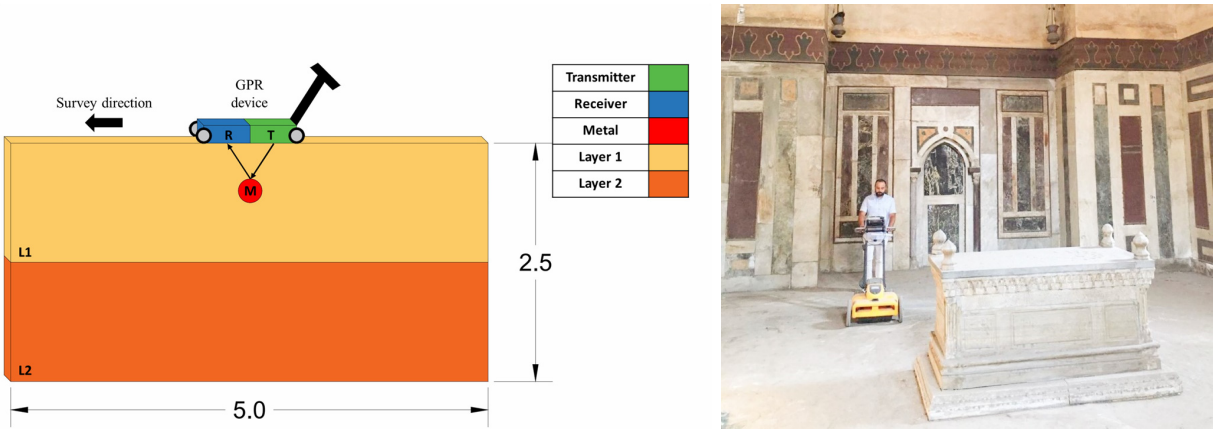


Figure 3. (**a**) A diagram of the ground-penetrating radar and (**b**) GPR measurements in Sorghatmesh mosque.

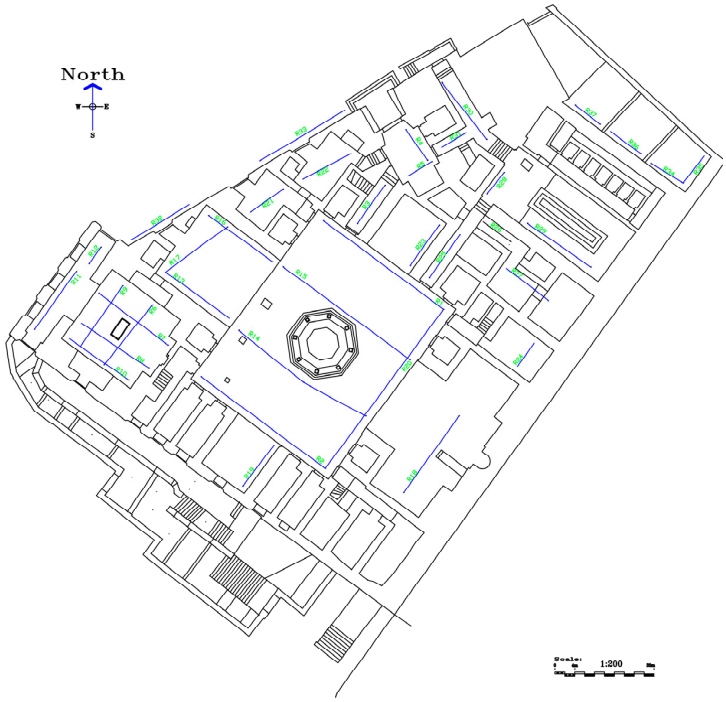


Figure 4. The ground floor of the Sorghatmesh mosque with the relative location of the 37 GPR lines (blue lines).

Prior to field measurements, the ground was cleared for the measurements, and test profile analyses were carried out to determine the optimum parameters for the GPR measurements (Table 1). Standard GPR signal processing functions were used for data corrections and optimization, including time zero correction to determine the accurate depths of objects, bandpass filtering to remove unwanted signal noises, and applying linear

and smooth gain functions to increase the amplitude of the reflected GPR wave signals (Table 2).

Table 1. GPR measurement parameters.

Depth Range	200 ns
Sample	512
Scan Step	0.03

Table 2. The applied GPR signal processing functions.

No.	Processing Function	Notes
1	Time zero correction	
2	Bandpass filtering	(300 to 900 for 700 MHz) (100 to 700 for 250 MHz)
3	Linear gain	
4	Smooth gain	

4. Data Interpretation

4.1. GPR Data Interpretation

The interpretation of the radargrams was conducted line by line. Each line has two radargrams which were interpreted simultaneously. Most of the 250 MHz and 700 MHz radargrams were visualized in blue and brown scales, respectively, for a better understanding of reflections. An interpreted example of the radargrams (radargram 1), along with its interpretation legend, is shown in Figure 5, with the presence of corroded rebar (at X = 5.8–7.6 m, Z = 0.3–0.55 m), reinforced concrete (at Z = 0.25–0.65 m), and rocks/concrete (at Z = 0.02–0.25 m) using the 700 MHz and the presence of two water/saturated zones (at X = 5.4–8.0 m, Z = 0.35–1.4 m and at X = 10.0–11.6 m, Z = 0.35–1.4), a sink drain (at X = 12.9 m), and an anomaly (at X = 2.8–7.6 m, Z = 6.9–7.2 m) using 250 MHz. The rest of the radargrams are provided in Appendix A.

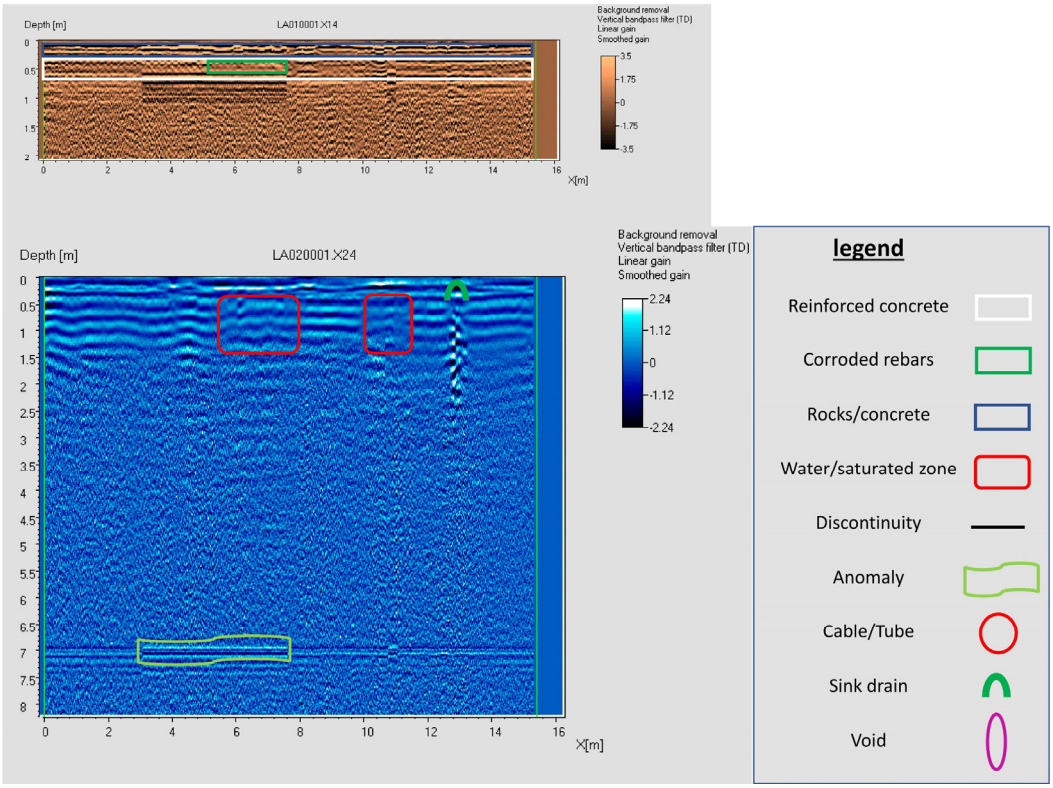


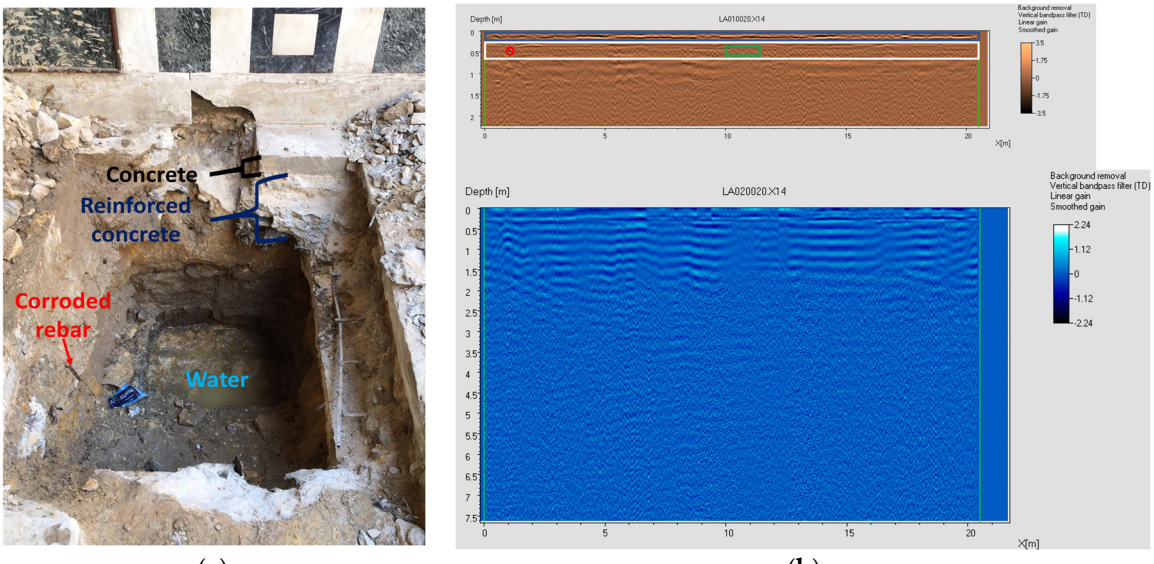
Figure 5. Results of radargram 1 with interpretation.

4.2. Trial Pit Validation

During the restoration work, an exploration trial pit was excavated on the ground floor of the mosque to visually investigate the subsurface content. We used this trial pit to validate our research. The location of the trial pit on the ground floor is shown in Figure 6; the closest radargrams to this trial pit were 14, 18, and 20. We found that the interpretation is coherent with the visual inspection of the trial pit (Figure 7).



Figure 6. The location of the trial pit (red color) relative to the lines of GPR (blue color).



(**a**) (**b**)

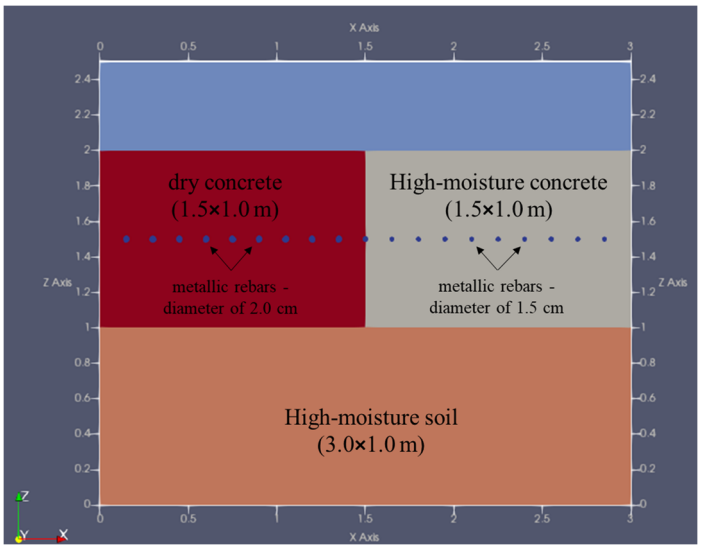
Figure 7. (**a**) The content of the trial pit and (**b**) the nearest radargram to the trial pit (radargram 14).

5. Georadar Simulation

A Georadar simulation was carried out using the open-source software gprMax Version 3.1.5 [50] which simulates the propagation of electromagnetic waves. This software package solves Maxwell's equations in 3D using the Finite Difference Time Domain (FDTD) method. The main purpose of the simulation process is to check the different responses that come from the subsurface materials and compare them with the measured GPR data at the site. The materials in the simulation model were considered according to the observation from the trial pit (Figure 7).

The model mainly consists of a combination of five main materials: dry concrete (ϵr = 8.0, σ = 0 S/m) at X = 0–1.5 m, Z = 1.0–2.0 m; high-moisture concrete (ϵr = 8.0, σ = 0.01 S/m) at X = 1.5–3.0 m, Z = 1.0–2.0 m; high-moisture soil (ϵr = 15.0, σ = 0.01 S/m) at Z = 0–1.0 m; metallic rebars (ϵr = 1.0, σ = ∞ S/m) embedded at Z = 1.5 m (the center point of rebars); and air (ϵr = 1.0, σ = 0 S/m) at Z = 2.0–2.5 m (Figure 8a). The model was built to simulate the responses of metallic rebars, the effect of corrosion, and the presence of moisture in concrete. The corrosion of rebars was simulated by them being embedded in high-moisture concrete and having a smaller diameter of 1.5 cm, while the other fit rebars had a 2.0 cm diameter and were embedded in dry concrete. The chosen frequency for simulation was 700 MHz (with a gaussiandotdotnorm waveform) to detect the changes in signal response. The GPR wave source and receiver are located at X = 0.02 m, Z = 2.0 m and X = 0.12 m, Z = 2.0 m, respectively, with a source–receiver step of 0.01 m.

The results of the simulation showed that there is a clear difference in the amplitudes of the reflected GPR waves between the fit rebars and the corroded rebars; the corroded rebars have weaker amplitudes than the fit rebars (Figure 8b). The simulation results also showed the effect of moisture on the GPR wave signal attenuation, leading to difficulty in detecting the soil layer underneath high-moisture concrete. The simulation results are well correlated with the actual GPR measurements at the site (radargram 16) (Figure 8c).



(**a**)

Figure 8. *Cont.*

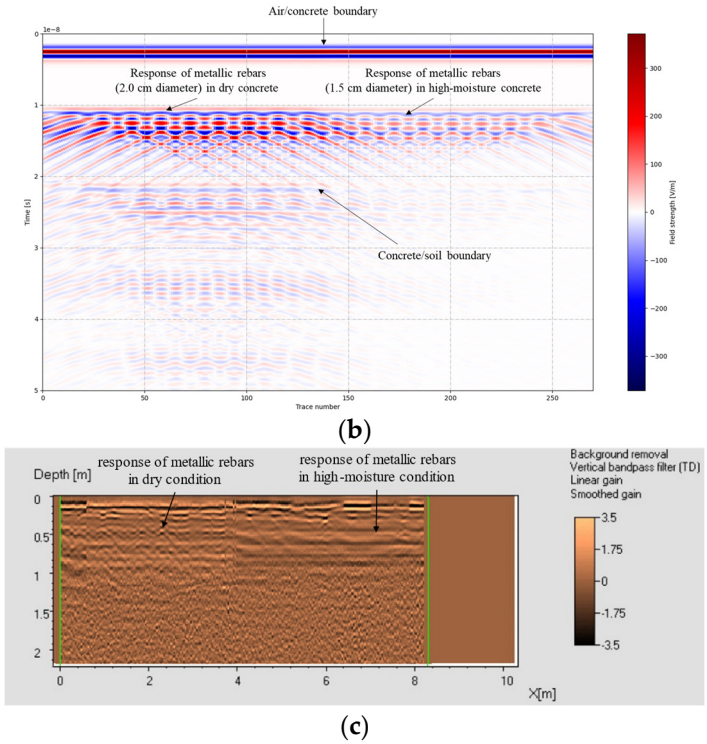


Figure 8. (**a**) The design of the Georadar simulation model; (**b**) the results of the simulation with interpretation; (**c**) the actual measured Georadar profile (radargram 16) with similar responses found by simulation.

6. Discussion

One of the main limitations presented in this study is the shallow depth of the groundwater level which led to the attenuation of the GPR waves especially for 700 MHz and the loss of the reflected EM signals due to the electrically conductive nature of groundwater. Such a limitation led to challenges and uncertainties in detecting and interpreting deep features.

The mosque's ground floor was divided into five main zones, A, B, C, D, and E (Table 3) (Figure 9), for a better comprehension of the results.

Table 3. Division zones with GPR radargrams for each zone.

Zone	GPR Lines
A	6,7,8,9,10,11,12
B	1,2,13,14,15,16,17,18,19,20
C	32,33
D	3,4,5,21,22,23,24,25,26,27,28,29,30,31
E	34,35,36,37

The radargrams showed that all the zones are affected by the presence of underground water at a depth ranging from 0.2 to 0.7 m, which led to the attenuation of the GPR signals. The subsurface medium inhomogeneity was a further cause of attenuation.

Radargrams at zone A detected a vertical anomaly in radargrams 6, 7, and 9, which could be a result of multiple reflections from a metal sink drain or void in the medium. The radargrams also detected a rock/concrete layer with a 20.0–25.0 cm thickness, under the ground surface, except for radargram 9 which detected a missing part of that layer. There was no sign of reinforced concrete presence. Radargram 6 detected the presence of a void with 1.0 m of vertical thickness, near the grave of Prince Sorghatmesh. In radargram 11, inclined rocks or blocks of concrete intersected with voids presented between them

(seeming to be stairways) were detected at a depth of 0.6 to 2.1 m with 2.0 m width. At the end of radargram 12, a reflected hyperbola was detected, which refers to a 3D body (cable/tube) at 0.55 m in depth.

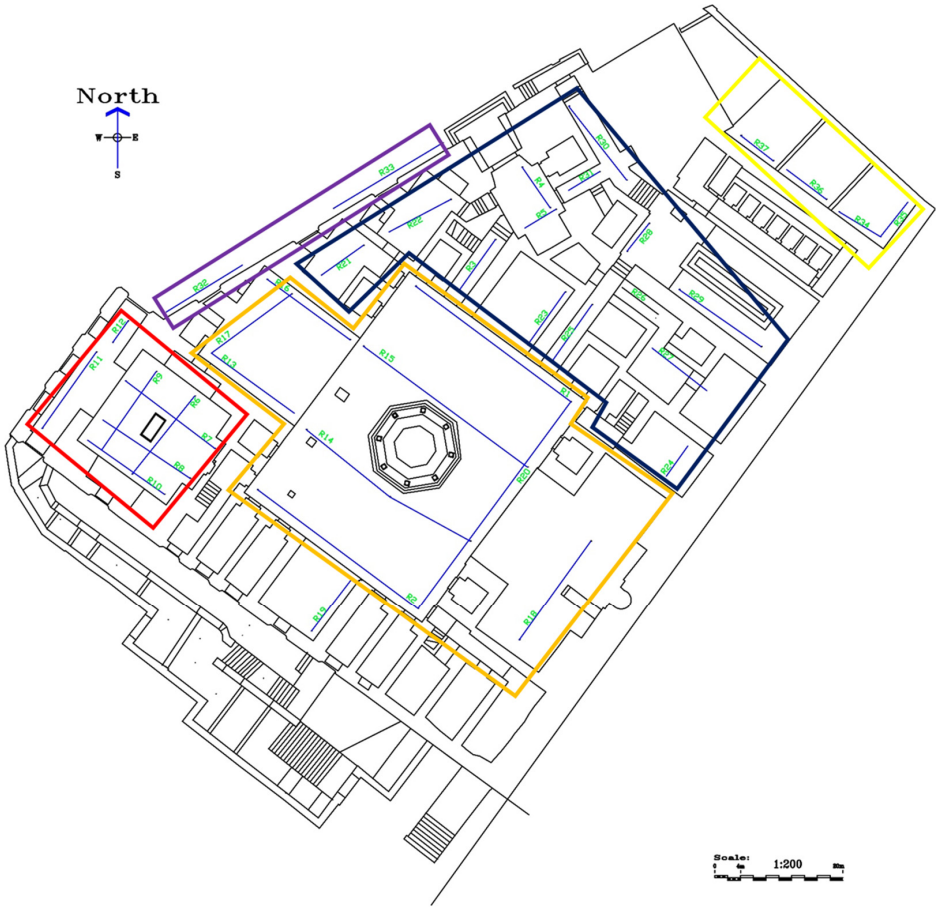


Figure 9. The five main zones of GPR measurements (GPR profiles are in blue) are zone A (red polygon), zone B (orange polygon), zone C (purple polygon), zone D (dark blue polygon), and zone E (yellow polygon).

Radargrams at zone B detected a concrete layer with 20.0–30.0 cm thickness followed by 30.0–40.0 cm of reinforced concrete, except for radargram 19, which did not detect reinforced concrete. Some of the radargrams (for example, 14-15-19-20) detected cables/tubes at the locations shown in the radargram figures. In this zone, a negative effect of groundwater on the construction materials of the subsurface was observed, which led to corrosion and unclear GPR signal reflections at shallow depths, as presented in most of the radargrams.

Radargrams at zone C detected a solid base that might be concrete. The reflections of this base were detected clearly at radargram 32, with a small inclination towards the mosque's main gate at a depth of 30.0 cm with a thickness of 60.0 cm. No clear signal was detected below 70.0 cm depth due to water presence. At radargram 33, a similar solid base was detected with lower amplitude reflection, probably because line 32 is closer than line 33 to that solid base.

Radargrams at zone D detected a concrete/rock layer with 20.0–25.0 cm thickness under the ground surface, except for radargram 29 which detected one with 58.0 cm thickness and radargram 27 which showed a partial loss for this layer. There was no sign of reinforced concrete. Many radargrams detected cables/tubes, as shown in radargrams 3, 6, 21, 23, 24, 25, and 28. Some of these cables/tubes were metals, as shown in radargrams 23 and 25. Some radargrams were highly affected by groundwater at shallow depths, which led to data masking at those parts (radargrams 3, 4, 25, 26, 27, 28, and 31). A curved

anomaly was detected in radargram 29 located at 1.2 m depth and 5.0 m length. At the end of radargram 31, a solid inclined body with 1.0 m length and 1.5 m depth was detected. Some radargrams detected discontinuities, as shown in radargrams 24, 25, and 29.

Radargrams at zone E detected a concrete/rock layer with about 20.0 cm thickness under the ground surface. At radargram 37, a metal body was detected near the ground surface which could have resulted from a sink drain. No further anomalies were detected in this zone.

In some radargrams, reflections of discontinuities at a depth of 7.0 m were detected in the area of a closed polygon (Figure 10). On these planes of discontinuity, there was a detected anomaly that could be a result of the ringing of a strong reflection from shallow bodies. The ringing was not detected in vertical connectivity as usual in radargrams which could be due to the presence of groundwater. The ringing was shown only at the deep discontinuity due to its strong reflection. This phenomenon requires engineering and geological checks to investigate the possibility of structure presence at this depth. The above-mentioned results provide important details about the subsurface current conditions, which represent crucial information allowing for the efficient restoration work of the structure.

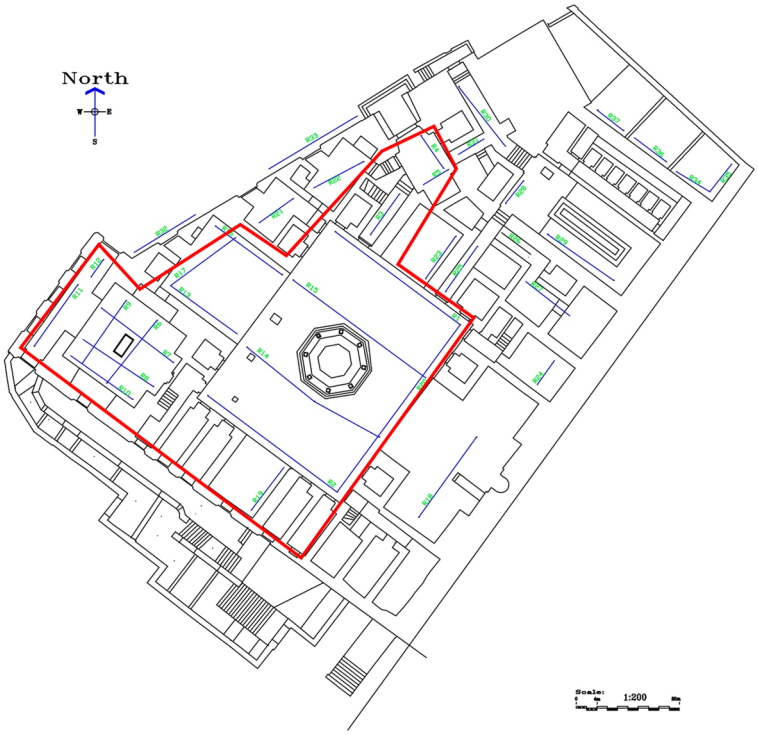


Figure 10. The discontinuity closed shape form (red polygon) with respect to GPR profiles (in blue).

7. Conclusions

GPR proved its ability as a geophysical non-destructive technique for the assessment of a subsurface. In this case study, a dual-frequency GPR (250–700 MHz) was used in a cultural heritage application, allowing for the subsurface investigation of Sorghatmesh mosque in Cairo for restoration purposes. Based on the interpretation of radargrams, the ground floor of the mosque was divided into five main zones (A, B, C, D, and E) for a better description and comprehension of the subsurface anomalies as the subsurface is non-uniform. The interpreted data were validated using a trial pit which allowed for a visual inspection of the subsurface medium and was supported by GPR numerical simulation, showing a clear correlation between GPR simulation and the on-site measurement results.

The results showed that all zones are affected by the presence of underground water at a depth ranging from 0.2 to 0.7 m, which led to signal attenuation and the corrosion of rebars in the subsurface reinforced concrete. Most radargrams in all zones detected a

concrete/rock layer with 20.0–58.0 cm thickness under the ground surface. The subsurface utilities (pipes, cables, sink drains) and subsurface structures were detected and interpreted in the radargrams. For example, in zone A, a void with 1.0 m vertical thickness near the grave of Prince Sorghatmesh and inclined blocks (which seem like stairways) at depth 0.6 to 2.1 m with 2.0 m width were detected. Most of the radargrams at zone B detected a 30.0–40.0 cm thickness of reinforced concrete beneath the rock/concrete layer, and this zone was highly affected by groundwater presence. At zone C, a solid base was detected that might be concrete with a slight inclination towards the mosque's main gate at a depth of 30.0 cm with a thickness of 60.0 cm. At zone D, a curved anomaly located at 1.2 m depth and 5.0 m length and a solid inclined body with 1.0 m length and 1.5 m depth were detected. Some radargrams were highly affected by groundwater at shallow depths as well. At zone E, a metal body that could be a sink drain was detected.

In some radargrams of different zones, reflections of planes of discontinuities at 7.0 m depth were detected. Interestingly, these radargrams were found in an area of a closed polygon which could be a reflection of a solid stratum. The present study requires a further geological investigation of the area and engineering action of the subsurface assessment. Some detected anomalies could be studied by archeologists. This study advances the methodology for the subsurface investigation of historical sites, illustrating how GPR simulations can improve the accuracy and reliability of subsurface assessments. The future work of this study includes the use of other non-destructive techniques including Ultrasonic testing and non-destructive ERT measurements, allowing for a further integrated effective approach.

Author Contributions: Formal analysis, M.E., H.E.A., K.H. and S.B.; investigation, M.E. and K.H.; methodology, M.E., H.E.A. and K.H.; project administration, M.E., F.A. and S.A.M.; resources, M.E. and K.H.; software, H.E.A. and K.H.; supervision, M.E., F.A. and S.A.M.; validation, F.A., S.B. and S.A.M.; visualization, H.E.A. and K.H.; writing—original draft, H.E.A.; writing—review and editing, M.E., H.E.A., S.B. and S.A.M. All authors have read and agreed to the published version of the manuscript.

Funding: This research received no external funding.

Data Availability Statement: The data presented in this study are available on request from the corresponding author and after obtaining the permission of the Ministry of Tourism and Antiquities.

Acknowledgments: We gratefully acknowledge the support of Ministry of Tourism and Antiquities for allowing and facilitating the field measurements. We would like to thank the Engineering Center for Archaeology and Environment (ECAE) in the Faculty of Engineering-Cairo University and the consultant of the Ministry of Tourism and Antiquities in the restoration project of Sorghatmesh mosque.

Conflicts of Interest: The authors declare no conflicts of interest.

Glossary of Technical Terms

Term	Definition
GPR, Georadar	The ground-penetrating radar device.
Radargram	The subsurface image obtained from the GPR device.
gprMax	An open-source library for 2D and 3D GPR wave simulation.
FDTD method	The Finite Difference Time Domain method is a numerical technique that solves Maxwell's equations in the time domain by discretizing space and time.

Appendix A

In this section, all measured radargrams (2–37) are presented along with their corresponding interpretations, as shown in Figures A1–A9. These figures provide a detailed visual representation of the subsurface conditions and structural features detected throughout the floor of Sorghatmesh mosque.

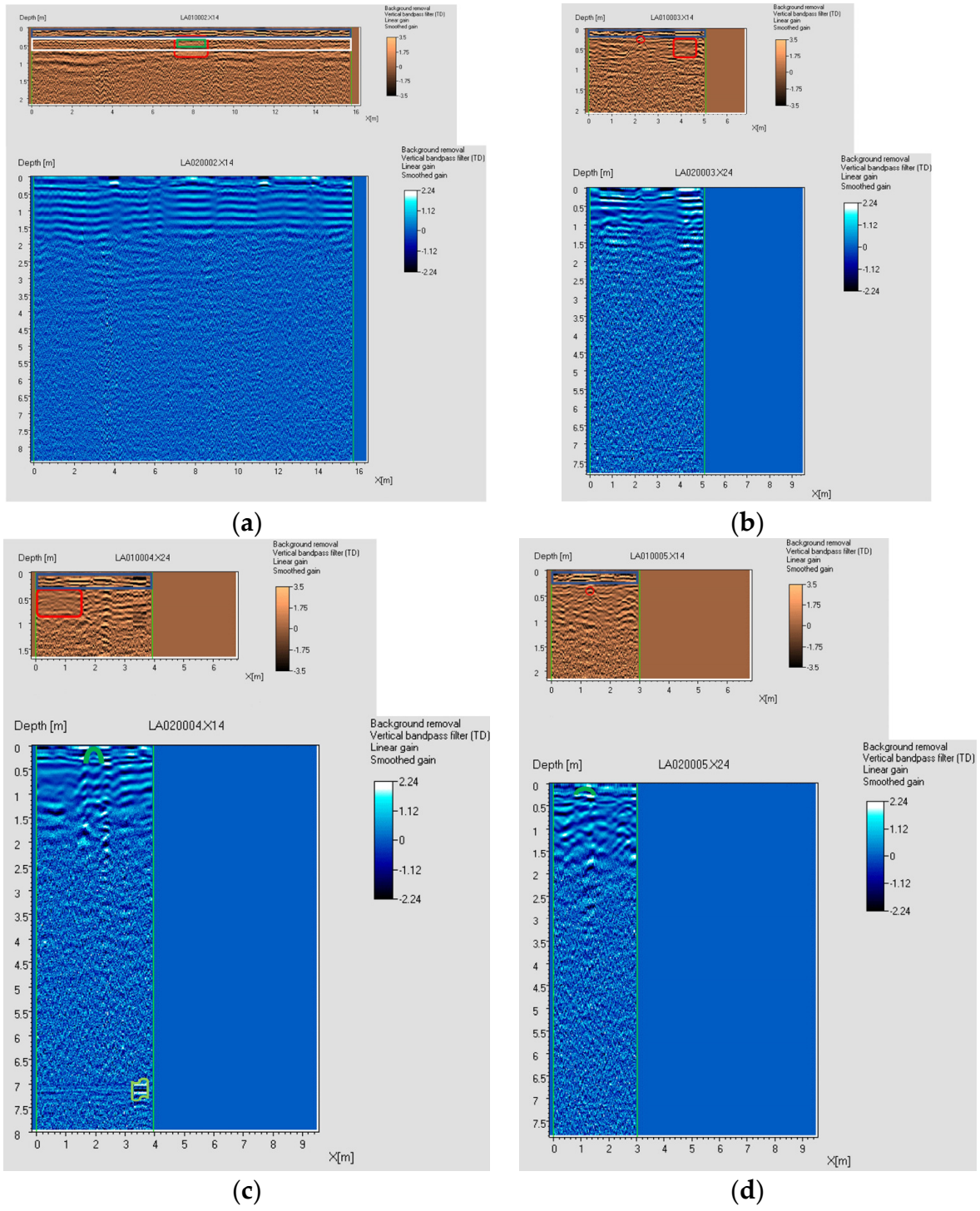


Figure A1. (**a**) Radargram 2 shows presence of corroded rebar (at X = 7.2–8.6 m, Z = 0.35–0.55 m), water/saturated zone (at X = 7.0–8.8 m, Z = 0.2–0.8 m), reinforced concrete (at Z = 0.25–0.6 m), and rocks/concrete (at Z = 0.02–0.25 m) (700 MHz). (**b**) Radargram 3 shows presence of water/saturated zones (at X = 3.6–4.7 m, Z = 0.2–0.7 m), cable/tube (at X = 2.2 m, Z = 0.25 m), and rocks/concrete (at Z = 0.02–0.2 m) (700 MHz). (**c**) Radargram 4 shows presence of water/saturated zone (at X = 0–1.6 m, Z = 0.3–0.85 m), rocks/concrete (at Z = 0.02–0.3 m) (700 MHz), sink drain (at X = 1.9 m), and anomaly (at X = 3.2–3.8 m, Z = 7.0–7.3 m) (250 MHz). (**d**) Radargram 5 shows presence of cable/tube (at X = 1.3 m, Z = 0.4 m), rocks/concrete (at Z = 0.02–0.25 m) (700 MHz), and sink drain (at X = 1.1 m, Z = 0.2 m) (250 MHz).

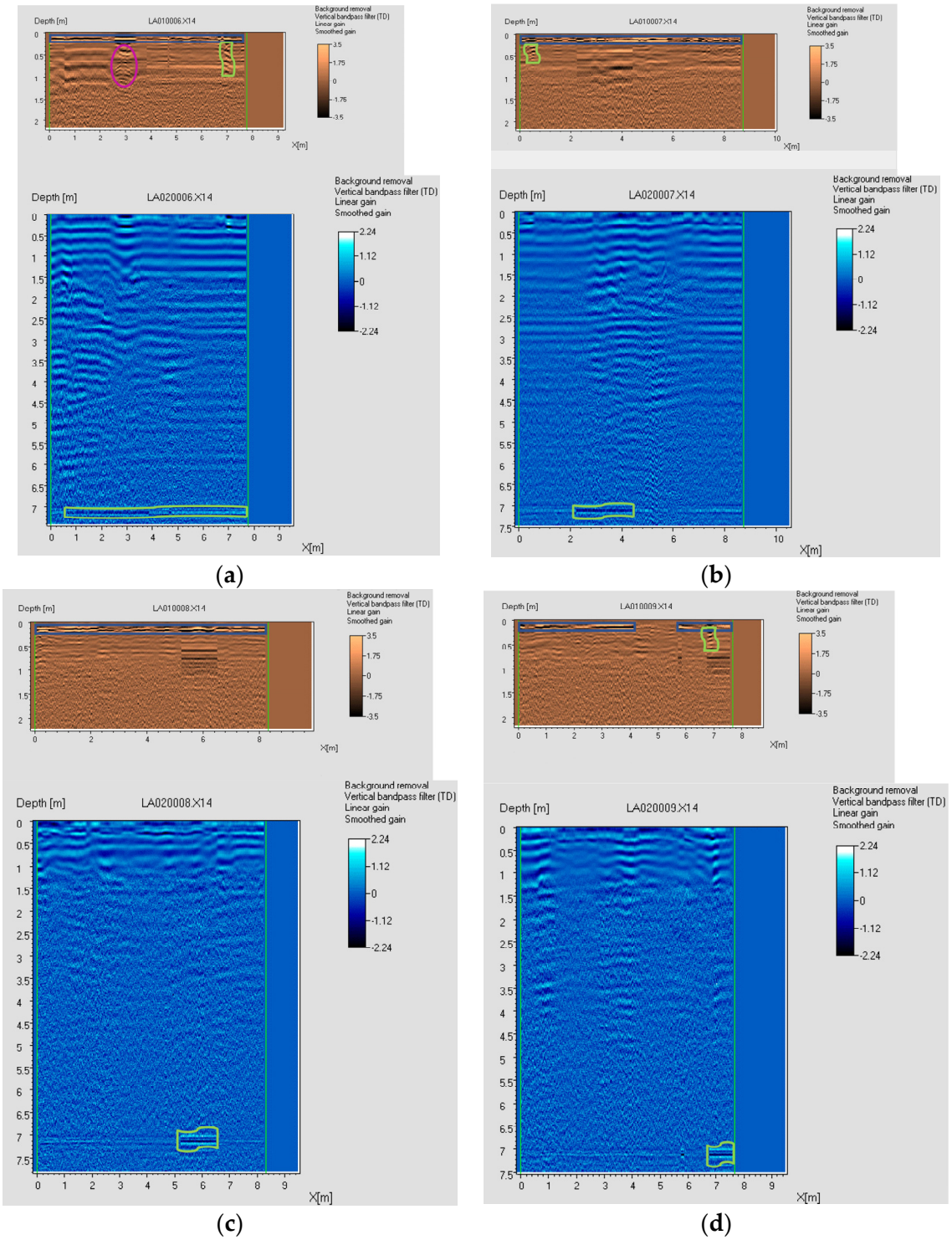


Figure A2. (**a**) Radargram 6 shows presence of void (at X = 3.0 m, Z = 0.3–1.3 m), anomaly (at X = 6.8–7.3 m, Z = 0.25–1.0 m), rocks/concrete (at Z = 0.02–0.25 m) (700 MHz), and anomaly (at X = 0.6–7.8 m, Z = 7.0–7.3 m) (250 MHz). (**b**) Radargram 7 shows presence of anomaly (at X = 0.3–0.7 m, Z = 0.2–0.7 m), rocks/concrete (at Z = 0.02–0.2 m) (700 MHz), and another anomaly (at X = 2.1–4.4 m, Z = 7.0–7.25 m) (250 MHz). (**c**) Radargram 8 shows presence of rocks/concrete (at Z = 0.02–0.2 m) (700 MHz) and anomaly (at X = 5.2–6.6 m, Z = 7.0–7.3 m) (250 MHz). (**d**) Radargram 9 shows presence of anomaly (at X = 6.7–7.1 m, Z = 0.1–0.6 m), rocks/concrete (at X = 0–4.2, Z = 0.02–0.2 m and at X = 5.7–7.6 m Z = 0.02–0.2 m) (700 MHz), and another anomaly (at X = 6.7–7.6 m, Z = 6.9–7.2 m) (250 MHz).

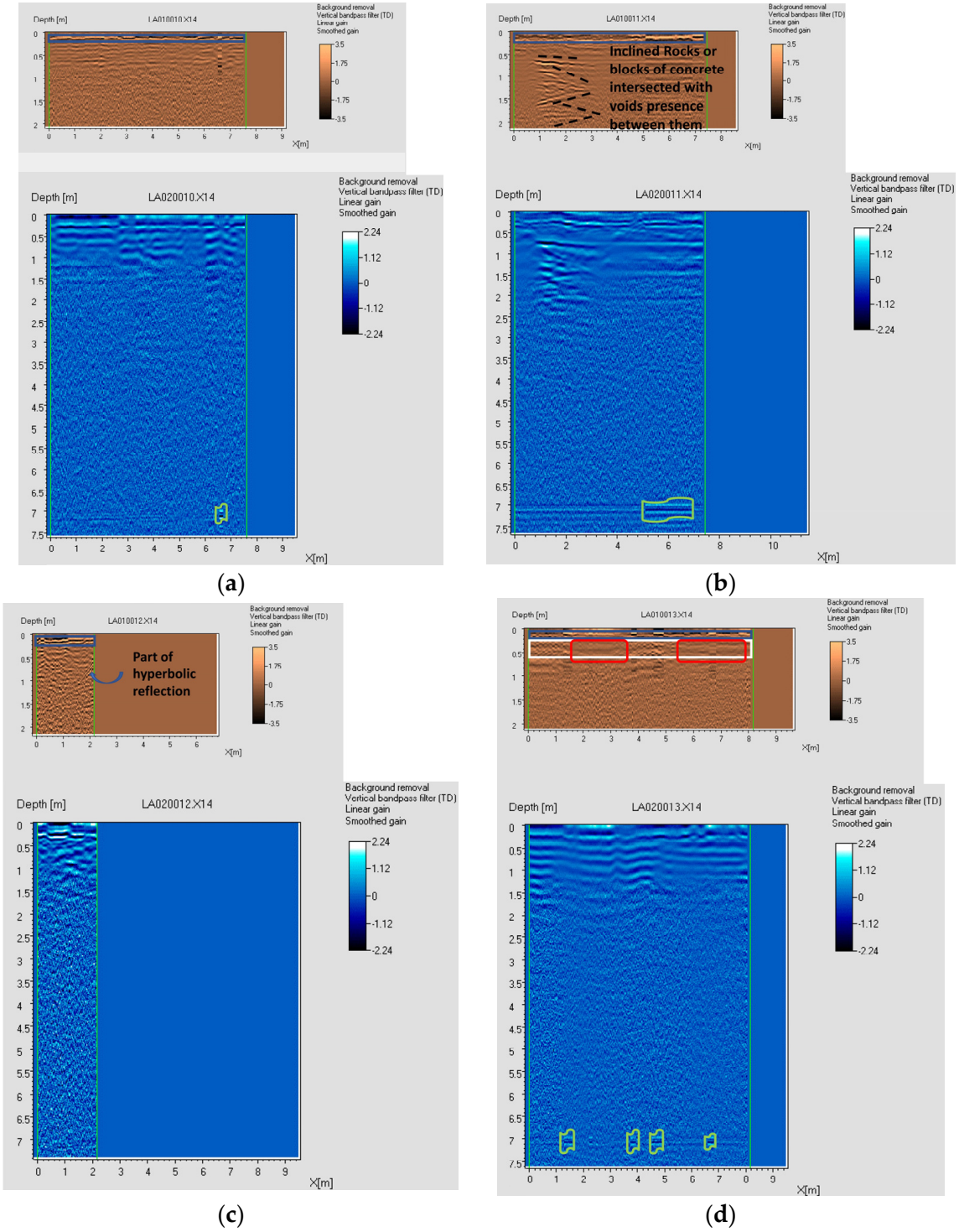


Figure A3. (**a**) Radargram 10 shows presence of rocks/concrete (at Z = 0.02–0.2 m) (700 MHz) and anomaly (at X = 6.5–6.8 m, Z = 6.9–7.2 m) (250 MHz). (**b**) Radargram 11 shows presence of inclined blocks of concrete intersected with void presence between them (at X = 0.8–3.1 m, Z = 0.6–2.1 m) (700–250 MHz), rocks/concrete (at Z = 0.02–0.2 m) (700 MHz), and anomaly (at X = 5.0–7.0 m, Z = 7.0–7.2 m) (250 MHz). (**c**) Radargram 12 shows presence of part of hyperbolic reflection (at X = 1.8–2.1 m, Z = 0.55 m) and rocks/concrete (at Z = 0.02–0.2 m) (700 MHz). (**d**) Radargram 13 shows presence of water/saturated zones (at X = 1.6–3.6 m, Z = 0.2–0.7 m, and X = 5.4–7.9 m, Z = 0.2–0.7 m), reinforced concrete (at Z = 0.2–0.6 m), rocks/concrete (at Z = 0.02–0.2 m) (700 MHz), and anomalies (at X = 1.2–1.6 m, Z = 7.0–7.2 m, at X = 3.6–4.0 m, Z = 7.0–7.2 m, at X = 4.5–5.0 m, Z = 7.0–7.2 m and at X = 6.5–6.9 m, Z = 7.0–7.2 m) (250 MHz).

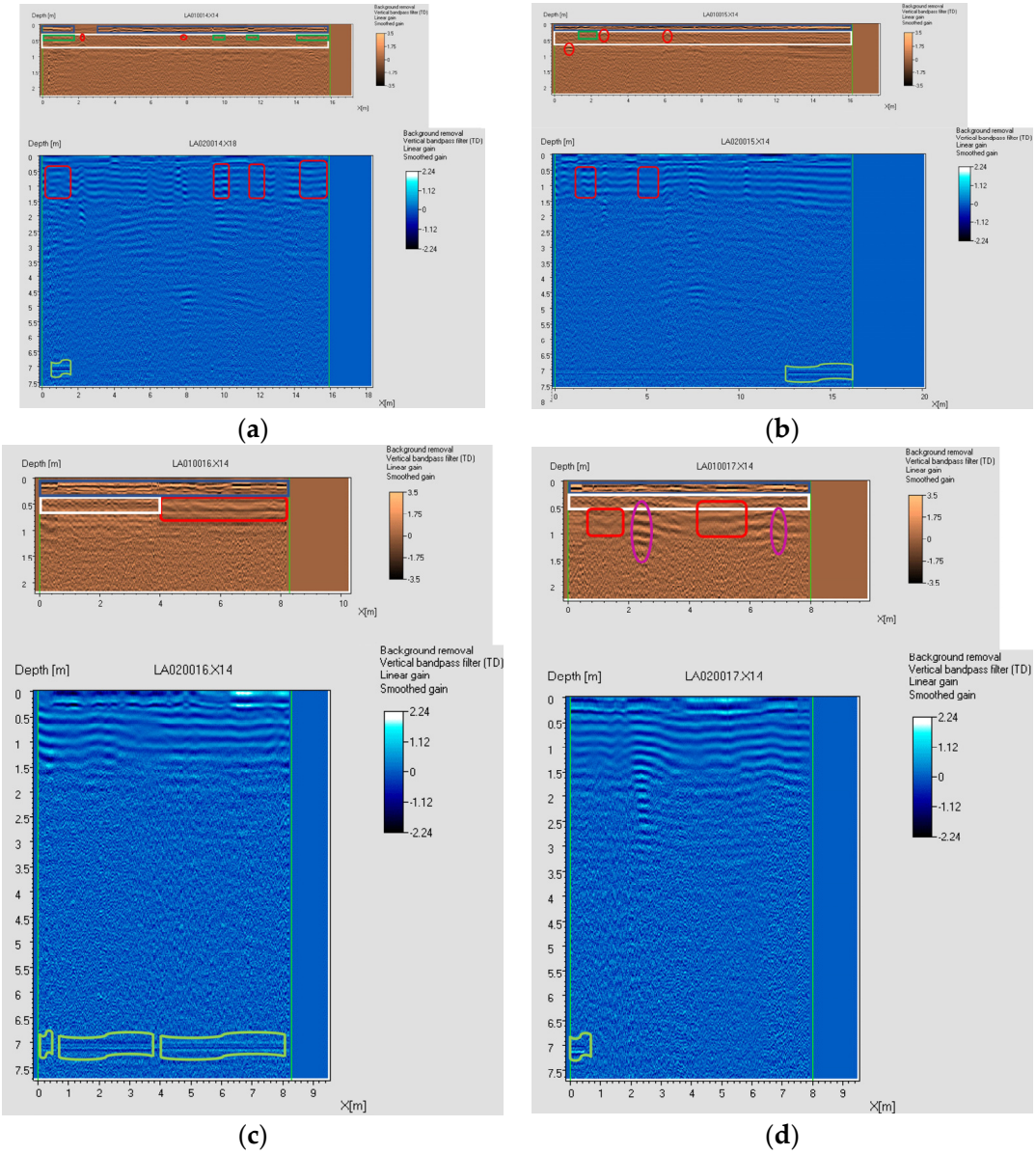


Figure A4. (**a**) Radargram 14 shows presence of corroded rebar (at X = 0–1.8 m, Z = 0.3–0.5 m, at X = 9.5–10.1 m, Z = 0.3–0.5 m, at X = 11.2–12.0 m, Z = 0.3–0.5 m, and at X = 14–15.8 m, Z = 0.3–0.5 m); cable/tube (at X = 2.2 m, Z = 0.45 m and at X = 7.8 m, Z = 0.45 m); reinforced concrete (at Z = 0.3–0.75 m); rocks/concrete (at X = 0–1.8, Z = 0.02–0.3 m, and at X = 3.0–15.8 m, Z = 0.02–0.3 m) (700 MHz); water/saturated zones (at X = 0.2–1.6 m, Z = 0.2–1.4 m, at X = 9.6–10.4 m, Z = 0.2–1.4 m, at X = 11.5–12.4 m, Z = 0.2–1.4 m, and at X = 14.4–15.8 m, Z = 0.1–1.4 m); and anomaly (at X = 0.4–1.6 m, Z = 7.0–7.2) (250 MHz). (**b**) Radargram 15 shows presence of corroded rebar (at X = 1.3–2.4 m, Z = 0.2–0.5 m); cable/tube (at X = 0.8 m, Z = 0.75 m, at X = 2.7 m, Z = 0.3 m, and at X = 6.15 m, Z = 0.3 m); reinforced concrete (at Z = 0.2–0.6 m); rocks/concrete (at Z = 0.02–0.2 m) (700 MHz); water/saturated zone (at X = 1.1–2.2 m, Z = 0.4–1.4 m, and at X = 4.5–5.6 m, Z = 0.4–1.4 m); and anomaly (at X = 12.7–16.0 m, Z = 7.0–7.4 m) (250 MHz). (**c**) Radargram 16 shows presence of water/saturated zone (at X = 4.0–8.2 m, Z = 0.3–0.8 m); reinforced concrete (at X = 0–4.0 m, Z = 0.3–0.65 m); rocks/concrete (at Z = 0.02–0.3 m) (700 MHz); and anomaly (at Z = 7.0–7.2 m) (250 MHz). (**d**) Radargram 17 shows presence of voids (at X = 2.4 m, Z = 0.35–1.5 m and at X = 6.9 m, Z = 0.5–1.35 m); water/saturated zones (at X = 0.6–1.8 m, Z = 0.5–1.0 m and at X = 4.2–5.9 m, Z = 0.35–1.0 m); reinforced concrete (at Z = 0.2–0.55 m); rocks/concrete (at Z = 0.02–0.2 m) (700 MHz); and anomalies (at X = 0–0.6 m, Z = 7.0–7.2 m) (250 MHz).

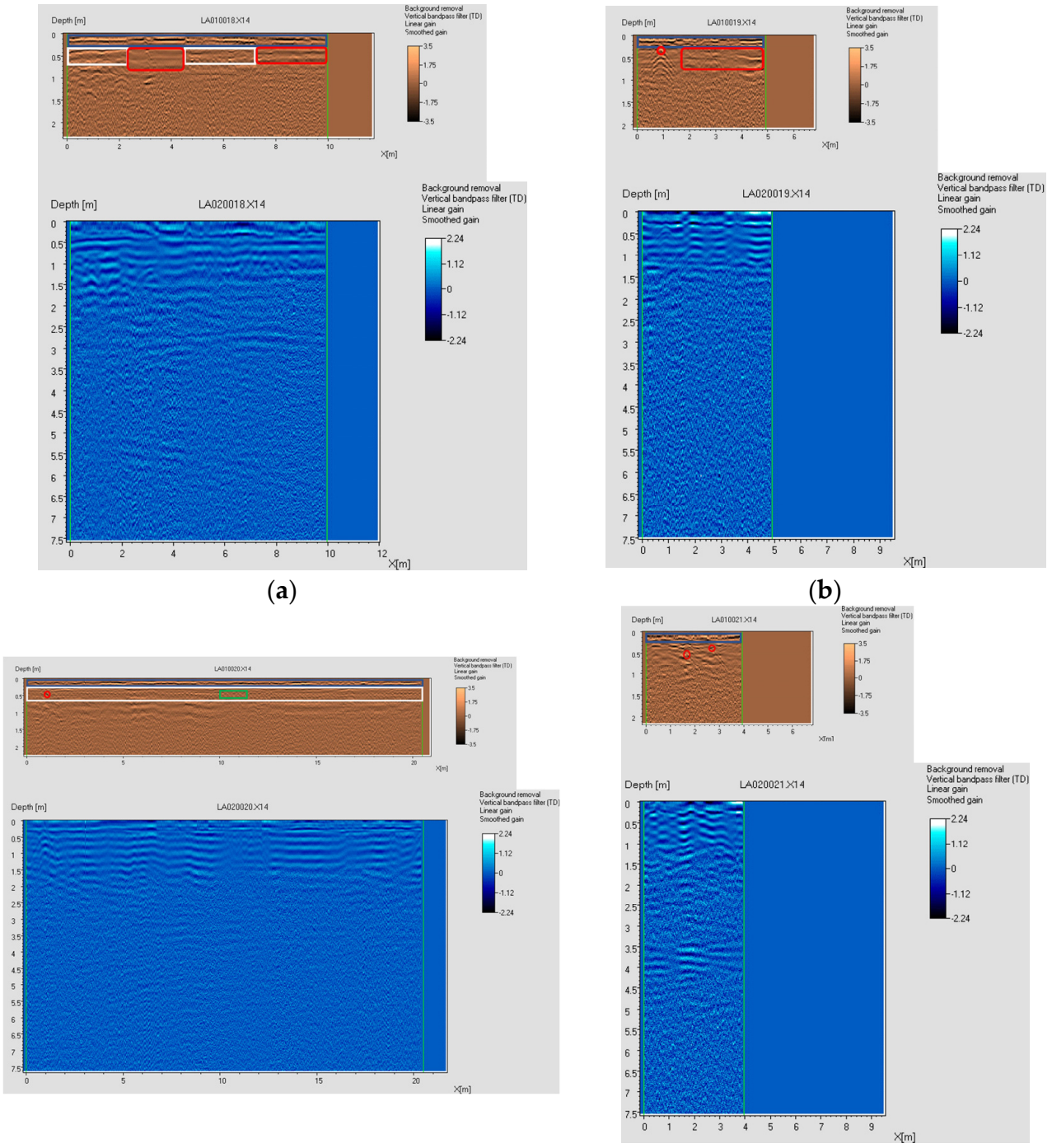


Figure A5. (**a**) Radargram 18 shows presence of water/saturated zones (at X = 2.4–4.4 m, Z = 0.3–0.8 m, and X = 7.2–10.0 m, Z = 0.3–0.65 m), reinforced concrete (at X = 0–2.4 m, Z = 0.3–0.65 m and at X = 4.4–7.2 m, Z = 0.3–0.65 m), and rocks/concrete (at Z = 0.02–0.3 m) (700 MHz). (**b**) Radargram 19 shows presence of cable/tube (at X = 0.9 m, Z = 0.3 m), water/saturated zone (at X = 1.7–4.8 m, Z = 0.25–0.75 m), and rocks/concrete (at Z = 0.02–0.25 m) (700 MHz). (**c**) Radargram 20 shows presence of cable/tube (at X = 1.0 m, Z = 0.45 m), corroded rebar (at X = 10.0–11.4 m, Z = 0.3–0.55 m), reinforced concrete (at Z = 0.2–0.6 m), and rocks/concrete (at Z = 0.02–0.2 m) (700 MHz). (**d**) Radargram 21 shows presence of cable/tube (at X = 1.7 m, Z = 0.5 m and at X = 2.7 m, Z = 0.35 m) and rocks/concrete (at Z = 0.02–0.2 m) (700 MHz).

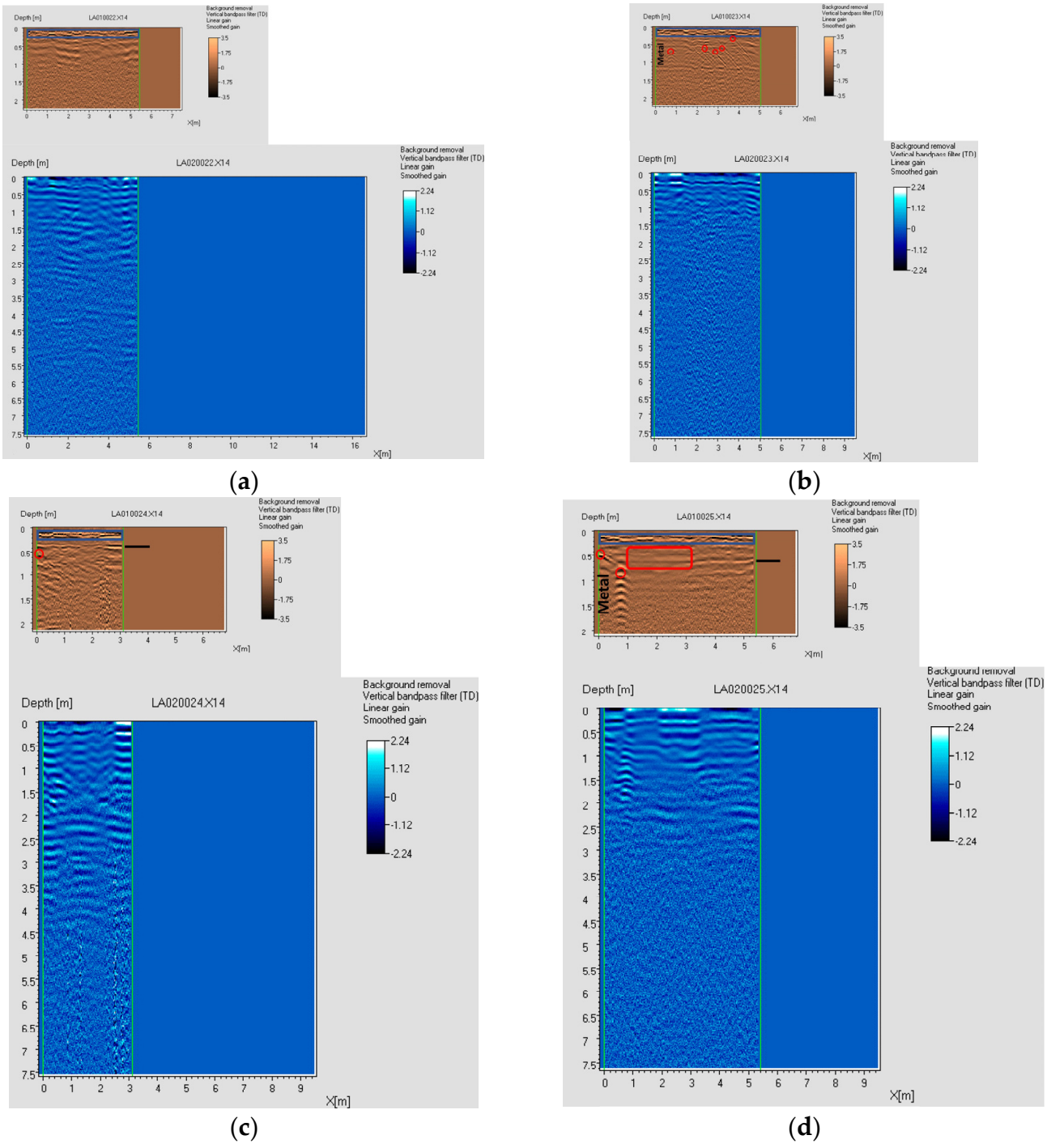


Figure A6. (**a**) Radargram 22 shows presence of rocks/concrete (at Z = 0.02–0.25 m) (700 MHz). (**b**) Radargram 23 shows presence of metallic object (at X = 0.8 m, Z = 0.7 m); cable/tube (at X = 2.4 m, Z = 0.6 m, X = 2.8 m, Z = 0.7 m, X = 3.2 m, Z = 0.6 m, and X = 3.7 m, Z = 0.3 m); and rocks/concrete (at Z = 0.02–0.25 m) (700 MHz). (**c**) Radargram 24 shows presence of cable/tube (at X = 0.1 m, Z = 0.55 m), discontinuity (at Z = 0.4), and rocks/concrete (at Z = 0.02–0.2 m) (700 MHz). (**d**) Radargram 25 shows presence of metallic object (at X = 0.75 m, Z = 0.8 m), cable/tube (at X = 0.1 m, Z = 0.5 m), water/saturated zones (at X = 1.0–3.2 m, Z = 0.3–0.75 m), discontinuity (at Z = 0.6 m), and rocks/concrete (at Z = 0.02–0.25 m) (700 MHz).

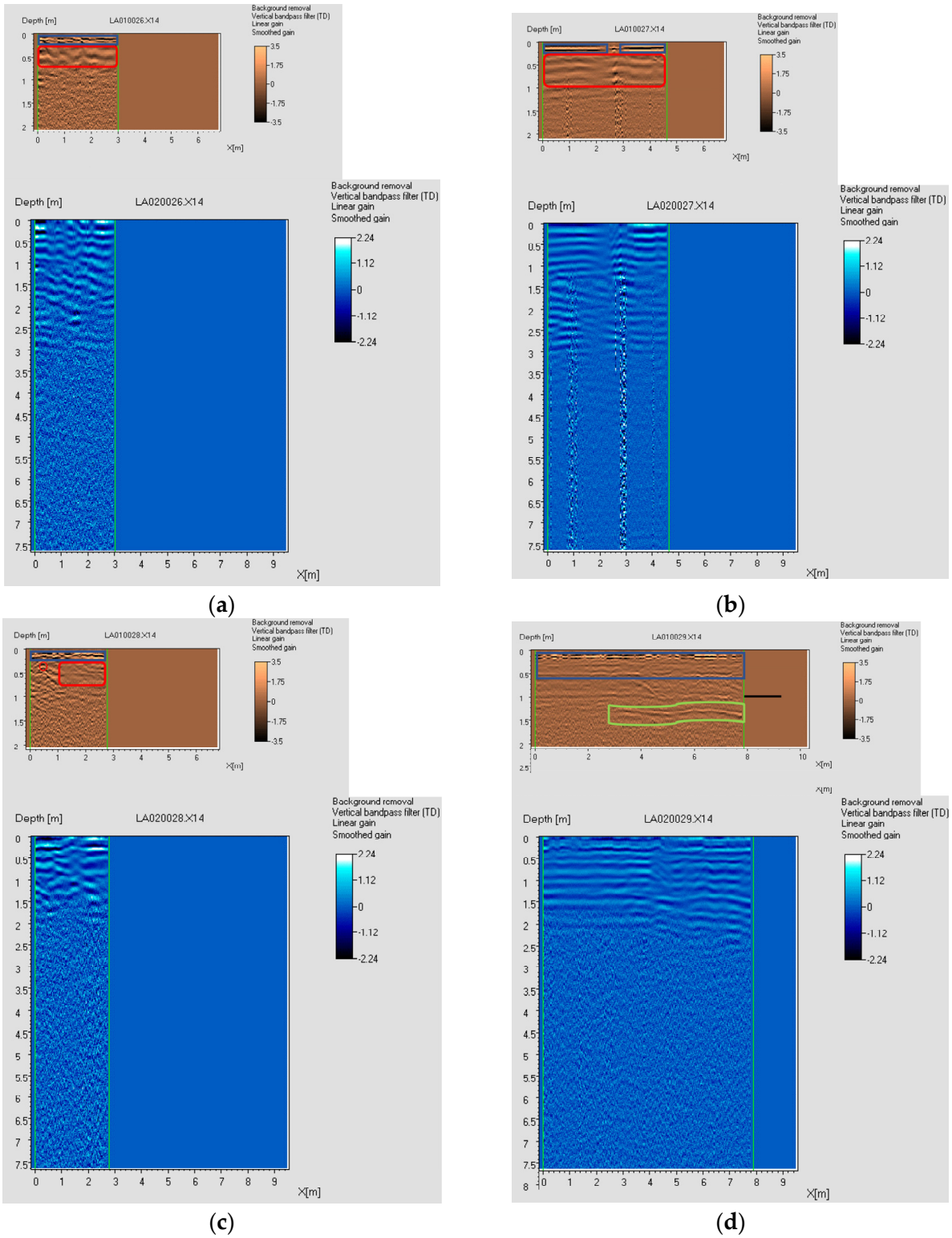


Figure A7. (**a**) Radargram 26 shows presence of water/saturated zone (at Z = 0.25–0.7 m) and rocks/concrete (at Z = 0.02–0.25 m) (700 MHz). (**b**) Radargram 27 shows presence of water/saturated zone (at Z = 0.2–1.0 m) and rocks/concrete (at X = 0–2.4 m, Z = 0.02–0.2 m and at X = 2.85–4.5 m, Z = 0.02–0.2 m) (700 MHz). (**c**) Radargram 28 shows presence of cable/tube (at X = 0.45 m, Z = 0.35 m), water/saturated zone (at X = 1.0–2.75 m, Z = 0.25–0.75 m), and rocks/concrete (at Z = 0.02–0.2 m) (700 MHz). (**d**) Radargram 29 shows presence of anomaly (at X = 2.8–7.8 m, Z = 1.2–1.5 m), discontinuity (at Z = 1.0 m), and rocks/concrete (at Z = 0.02–0.6 m) (700 MHz).

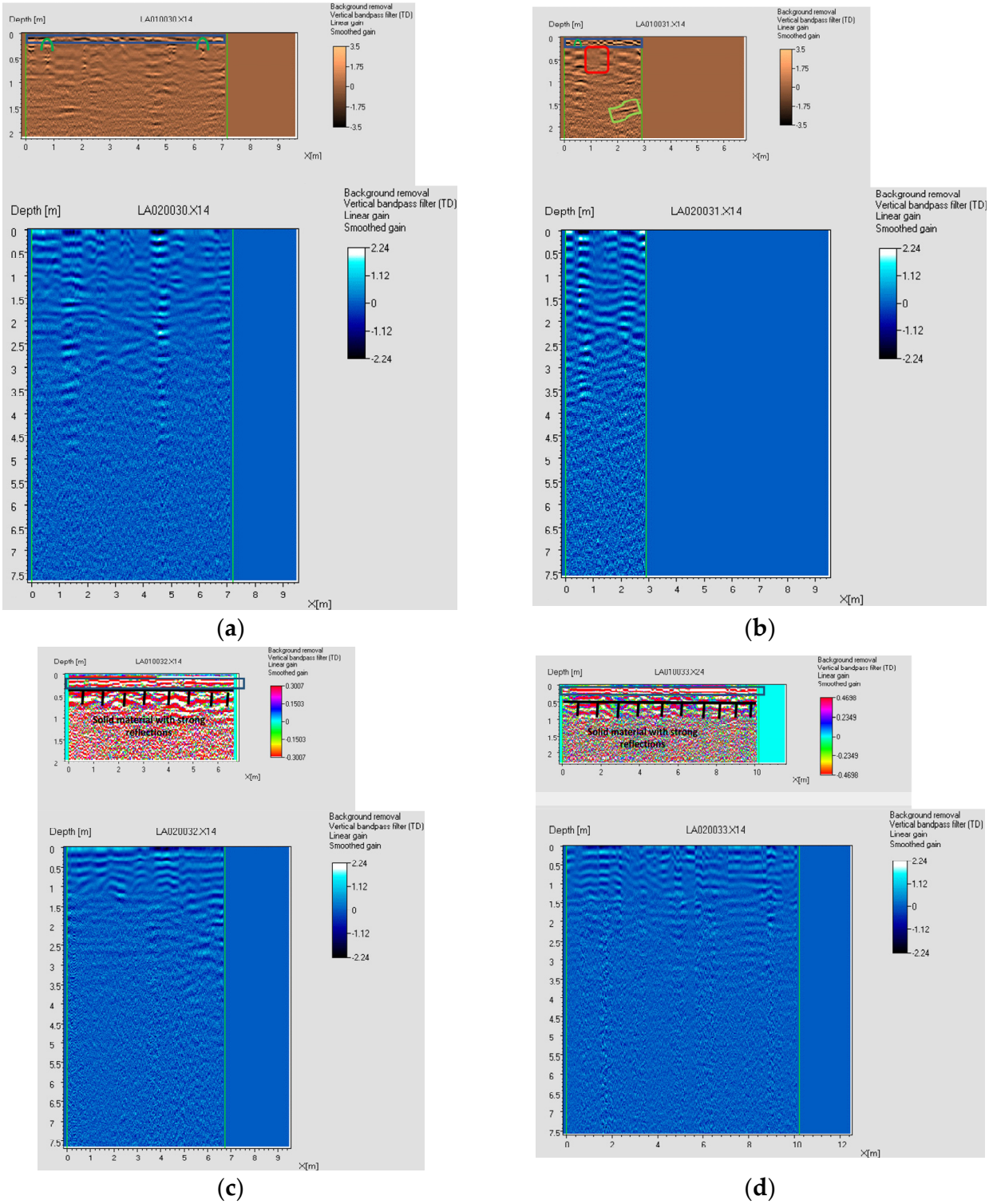


Figure A8. (**a**) Radargram 30 shows presence of sink drains (at X = 0.8 m and X = 6.4 m) and rocks/concrete (at Z = 0.02–0.2 m) (700 MHz). (**b**) Radargram 31 shows presence of sink drain (at X = 0.55 m), water/saturated zone (at X = 0.8–1.6 m, Z = 0.2–0.8 m), anomaly (at X = 1.8–2.8 m, Z = 1.5–1.75 m), and rocks/concrete (at Z = 0.02–0.2 m) (700 MHz). (**c**) Radargram 32 shows presence of strong reflection from solid material (at Z = 0.3–0.9 m) and rocks/concrete (at Z = 0.08–0.3 m) (700 MHz). (**d**) Radargram 33 shows presence of strong reflection from solid material (at Z = 0.4–0.8 m) and rocks/concrete (at Z = 0.05–0.3 m) (700 MHz).

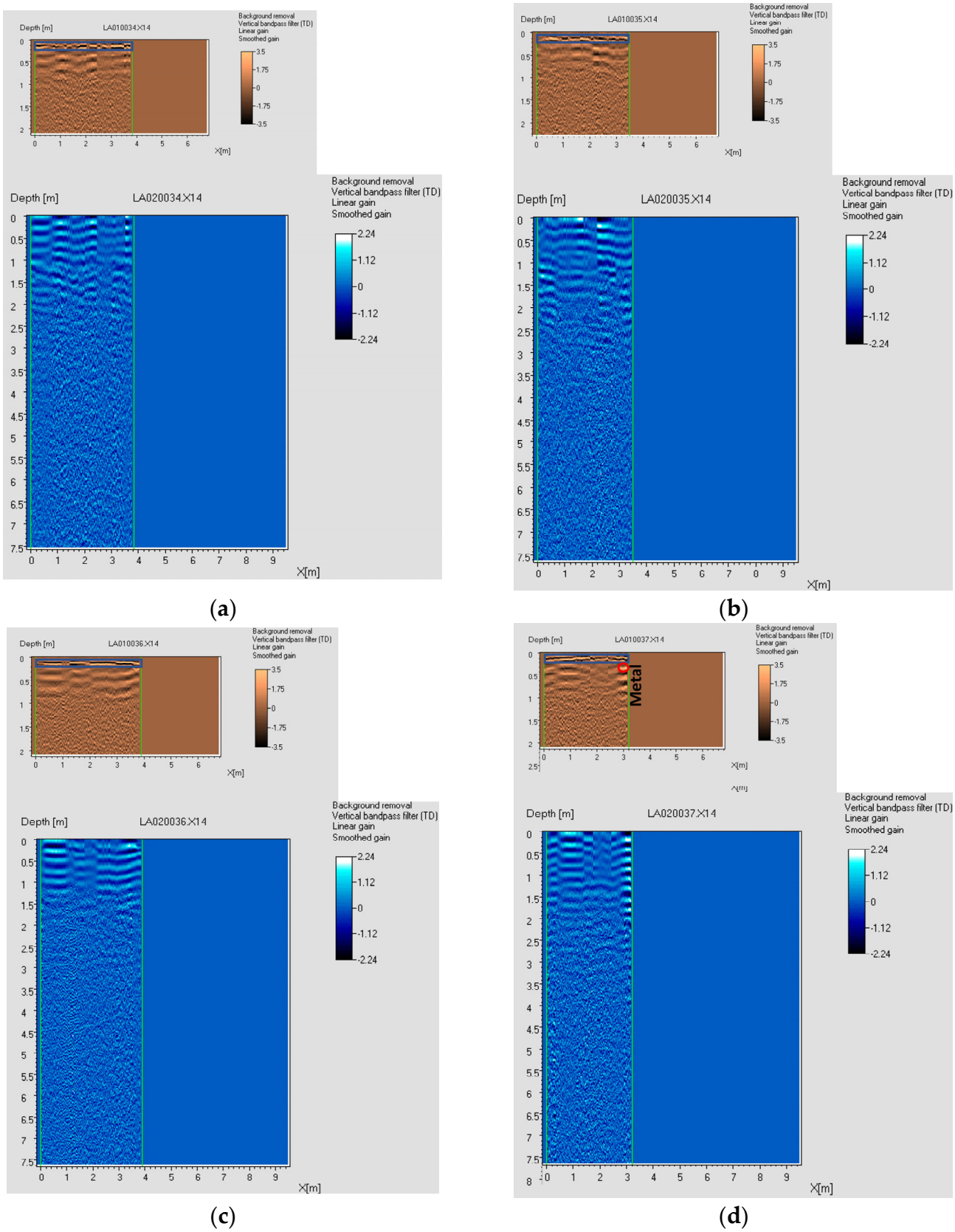


Figure A9. (**a**) Radargram 34 shows presence of rocks/concrete (at Z = 0.02–0.2 m) (700 MHz). (**b**) Radargram 35 shows presence of and rocks/concrete (at Z = 0.02–0.2 m) (700 MHz). (**c**) Radargram 36 shows presence of rocks/concrete (at Z = 0.02–0.2 m) (700 MHz). (**d**) Radargram 37 shows presence of anomaly (at X = 3.0 m, Z = 0.3 m) and rocks/concrete (at Z = 0.02–0.2 m) (700 MHz).

References

1. Abd al-Wahab, H. *Book of Tarikh al-Masajid al-Athariya bil Qahira [History of Monumental Mosques in Cairo]*; Egyptian General Authority for Books: Cairo, Egypt, 1994.
2. Al-Maqrizi. *Al-mawāʻiz waʼl-iʼtibār bi-dhikr al-khiṭaṭ waʼl-āthār [Exhortations and Contemplation of the Recollection of Plans and Monuments]*; 2 Volumes; Dār al-Ṭibāʻah al-Misṛīyah: Cairo, Egypt, 1853.
3. Walker, B.J. On Archives and Archaeology: Reassessing Mamluk Rule from Documentary Sources and Jordanian Fieldwork. In *Material Evidence and Narrative Sources: Interdisciplinary Studies of the History of the Muslim Middle East*; Talmon-Heller, D., Cytryn-Silverman, K., Eds.; Brill: Leiden, The Netherlands, 2015; p. 120.
4. Salem, a.-S.M.A.a.-A. *al-Maʼdin al-Masriya-Nazra ʻAmma ʻan aslaha wa tatawuriha mundu al-fath al-ʻarabi hatta al-fath al-Othmani [The Egyptian Minaret—A General View of Its Origin and Development from the Arab Conquest until the Ottoman Conquest]*; General Authority for Government Printing Offices: Cairo, Egypt, 1959.
5. Creswell, K.A.C. *Muslim Architecture of Egypt*; Hacker Art Books: New York, NY, USA, 1960; Volume 2.
6. Behrens-Abouseif, D. *Islamic Architecture in Cairo*; Brill: Leiden, The Netherlands, 1989.
7. Jarrar, S.; Riedlmayer, A.; Spurr, J.B. *Resources for the Study of Islamic Architecture*; Aga Khan Program for Islamic Architecture: Cambridge, MA, USA, 1994.
8. Kessler, C. Funerary Architecture within the City. In *Colloque International Sur L'histoire du Caire*; Ministry of Culture of the Arab Republic of Egypt: Cairo, Egypt, 1969; pp. 385–403.
9. Elkarmoty, M.; Colla, C.; Gabrielli, E.; Papeschi, P.; Bonduà, S.; Bruno, R. In-situ GPR test for three-dimensional mapping of the dielectric constant in a rock mass. *J. Appl. Geophys.* **2017**, *146*, 1–15. [CrossRef]
10. Annan, A.P. *Ground Penetrating Radar Principles, Procedures, and Applications*; Sensors & Software: Mississauga, ON, Canada, 2003.
11. Elkarmoty, M.; Tinti, F.; Kasmaeeyazdi, S.; Bonduà, S.; Bruno, R. 3D modeling of discontinuities using GPR in a commercial size ornamental limestone block. *Constr. Build. Mater.* **2018**, *166*, 81–86. [CrossRef]
12. Daniels, D.J. *Ground Penetrating Radar*; The Institute of Electrical Engineers: London, UK, 2004.
13. Elkarmoty, M.; Colla, C.; Gabrielli, E.; Bonduà, S.; Bruno, R. Deterministic three-dimensional rock mass fracture modeling from geo-radar survey: A case study in a sandstone quarry in Italy. *Environ. Eng. Geosci.* **2017**, *23*, 314–331. [CrossRef]
14. Reynolds, J.M. *An Introduction to Applied and Environmental Geophysics*; John Wiley & Sons, Ltd.: West Sussex, UK, 2011.
15. Elkarmoty, M.; Tinti, F.; Kasmaeeyazdi, S.; Giannino, F.; Bonduà, S.; Bruno, R. Implementation of a Fracture Modeling Strategy Based on Georadar Survey in a Large Area of Limestone Quarry Bench. *Geosciences* **2018**, *8*, 481. [CrossRef]
16. Yelfm, R.J. Application of ground penetrating radar to civil and geotechnical engineering. *Electromagn. Phenom.* **2007**, *7*, 103–117.
17. Elkarmoty, M.; Colla, C.; Gabrielli, E.; Bonduà, S.; Bruno, R. Application of low frequency GPR antenna to fractures detection and 3D visualization in a new quarry bench (E-poster). In Proceedings of the International Conference on Geophysics, Orlando, CO, USA, 6–7 October 2016.
18. Sambuelli, L.; Comina, C.; Catanzariti, G.; Barsuglia, F.; Morelli, G.; Porcelli, F. The third KV62 radar scan: Searching for hidden chambers adjacent to Tutankhamun's tomb. *J. Cult. Herit.* **2019**, *39*, 288–296. [CrossRef]
19. Ranalli, D.; Scozzafava, M.; Tallini, M. Ground penetrating radar investigations for the restoration of historic buildings: The case study of the Collemaggio Basilica (L'Aquila, Italy). *J. Cult. Herit.* **2004**, *5*, 91–99. [CrossRef]
20. Novo, A.; Solla, M.; Fenollós, J.L.M.; Lorenzo, H. Searching for the remains of an Early Bronze Age city at Tell Qubr Abu al-'Atiq (Syria) through archaeological investigations and GPR imaging. *J. Cult. Herit.* **2014**, *15*, 575–579. [CrossRef]
21. Barilaro, D.; Branca, C.; Gresta, S.; Imposa, S.; Leone, A.; Majolino, D. Ground penetrating radar (GPR) surveys applied to the research of crypts in San Sebastiano's church in Catania (Sicily). *J. Cult. Herit.* **2007**, *8*, 73–76. [CrossRef]
22. Pérez-Gracia, V.; García, F.; Pujades, L.G.; Drigo, R.G.; Di Capua, D. GPR survey to study the restoration of a Roman monument. *J. Cult. Herit.* **2008**, *9*, 89–96. [CrossRef]
23. Deiana, R. The contribution of geophysical prospecting to the multidisciplinary study of the Sarno Baths, Pompeii. *J. Cult. Herit.* **2019**, *40*, 274–279. [CrossRef]
24. Russo, S. Integrated assessment of monumental structures through ambient vibrations and ND tests: The case of Rialto Bridge. *J. Cult. Herit.* **2016**, *19*, 402–414. [CrossRef]
25. D'Aranno, P.J.; De Donno, G.; Marsella, M.; Orlando, L.; Renzi, B.; Salviani, S.; Santarelli, M.L.; Scifoni, S.; Sonnessa, A.; Verri, F.; et al. High-resolution geomatic and geophysical techniques integrated with chemical analyses for the characterization of a Roman wall. *J. Cult. Herit.* **2016**, *17*, 141–150. [CrossRef]
26. Moropoulou, A.; Bakolas, A.; Karoglou, M.; Delegou, E.T.; Labropoulos, K.C.; Katsiotis, N.S. Diagnostics and protection of Hagia Sophia mosaics. *J. Cult. Herit.* **2013**, *14*, e133–e139. [CrossRef]
27. Puente, I.; Solla, M.; Lagüela, S.; Sanjurjo-Pinto, J. Reconstructing the Roman Site "Aquis Querquennis" (Bande, Spain) from GPR, T-LiDAR and IRT Data Fusion. *Remote Sens.* **2018**, *10*, 379. [CrossRef]
28. Leucci, G.; Persico, R.; Soldovieri, F. Detection of fractures from GPR data: The case history of the Cathedral of Otranto. *J. Geophys. Eng.* **2007**, *4*, 452–461. [CrossRef]
29. Neubauer, W.; Eder-Hinterleitner, A.; Seren, S.; Melichar, P. Georadar in the Roman civil town Carnuntum, Austria: An approach for archaeological interpretation of GPR data. *Archaeol. Prospect.* **2002**, *9*, 135–156. [CrossRef]
30. Abbas, A.M.; Kamei, H.; Helal, A.; Atya, M.A.; Shaaban, F.A. Contribution of geophysics to outlining the foundation structure of the Islamic Museum, Cairo, Egypt. *Archaeol. Prospect.* **2005**, *12*, 167–176. [CrossRef]

31. Cataldo, R.; D'Agostino, D.; Leucci, G. Insights into the Buried Archaeological Remains at the Duomo of Lecce (Italy) Using Ground-penetrating Radar Surveys. *Archaeol. Prospect.* **2012**, *19*, 157–165. [CrossRef]
32. Leucci, G.; Di Giacomo, G.; Ditaranto, I.; Miccoli, I.; Scardozzi, G. Integrated Ground-penetrating Radar and Archaeological Surveys in the Ancient City of Hierapolis of Phrygia (Turkey). *Archaeol. Prospect.* **2013**, *20*, 285–301. [CrossRef]
33. Teixidó, T.; Peña, J.A.; Fernández, G.; Burillo, F.; Mostaza, T.; Zancajo, J. Ultradense Topographic Correction by 3D-Laser Scanning in Pseudo-3D Ground-penetrating Radar Data: Application to the Constructive Pattern of the Monumental Platform at the Segeda I Site (Spain). *Archaeol. Prospect.* **2014**, *21*, 113–123. [CrossRef]
34. Matera, L.; Persico, R.; Bianco, N.; Leopizzi, G.; Leopizzi, G. Joined Interpretation of Buried Anomalies from Ground Penetrating Radar Data and Endoscopic Tests. *Archaeol. Prospect.* **2016**, *23*, 301–309. [CrossRef]
35. Ribolini, A.; Bini, M.; Isola, I.; Coschino, F.; Baroni, C.; Salvatore, M.C.; Zanchetta, G.; Fornaciari, A. GPR versus Geoarchaeological Findings in a Complex Archaeological Site (Badia Pozzeveri, Italy). *Archaeol. Prospect.* **2017**, *24*, 141–156. [CrossRef]
36. Utsi, E.C.; Colls, K.S. The GPR Investigation of the Shakespeare Family Graves. *Archaeol. Prospect.* **2017**, *24*, 335–352. [CrossRef]
37. Bianchini Ciampoli, L.; Santarelli, R.; Loreti, E.M.; Ten, A.; Benedetto, A. Structural detailing of buried Roman baths through GPR inspection. *Archaeol. Prospect.* **2020**, *30*, 3–11. [CrossRef]
38. Pieraccini, M.; Miccinesi, L.; Conti, A.; Fiorini, L.; Tucci, G.; Pieri, I.; Corazzini, S. Integration of GPR and TLS for investigating the floor of the 'Salone dei Cinquecento' in Palazzo Vecchio, Florence, Italy. *Archaeol. Prospect.* **2020**, *30*, 27–32. [CrossRef]
39. De Giorgi, L.; Lazzari, M.; Leucci, G.; Persico, R. Geomorphological and non-destructive GPR survey for the conservation of frescos in the rupestrian churches of Matera (Basilicata, southern Italy). *Archaeol. Prospect.* **2020**, *30*, 47–55. [CrossRef]
40. Feng, J.; Siegler, M.A.; White, M.N. Shallow Regolith Structure and Obstructions Detected by Lunar Regolith Penetrating Radar at Chang'E-5 Drilling Site. *Remote Sens.* **2022**, *14*, 3378. [CrossRef]
41. Jaufer, R.M.; Ihamouten, A.; Goyat, Y.; Todkar, S.S.; Guilbert, D.; Assaf, A.; Dérobert, X. A Preliminary Numerical Study to Compare the Physical Method and Machine Learning Methods Applied to GPR Data for Underground Utility Network Characterization. *Remote Sens.* **2022**, *14*, 1047. [CrossRef]
42. Guo, S.; Xu, Z.; Li, X.; Zhu, P. Detection and Characterization of Cracks in Highway Pavement with the Amplitude Variation of GPR Diffracted Waves: Insights from Forward Modeling and Field Data. *Remote Sens.* **2022**, *14*, 976. [CrossRef]
43. Hong, S.; Chen, D.; Dong, B. Numerical simulation and mechanism analysis of GPR-based reinforcement corrosion detection. *Constr. Build. Mater.* **2022**, *317*, 125913. [CrossRef]
44. Wong, P.T.; Lai, W.W. Characterization of Complex Dielectric Permittivity of Concrete by GPR Numerical Simulation and Spectral Analysis. *J. Nondestruct. Eval.* **2022**, *41*, 1. [CrossRef]
45. Puntu, J.M.; Chang, P.-Y.; Lin, D.-J.; Amania, H.H.; Doyoro, Y.G. A Comprehensive Evaluation for the Tunnel Conditions with Ground Penetrating Radar Measurements. *Remote Sens.* **2021**, *13*, 4250. [CrossRef]
46. Liu, S.; Lu, Q.; Li, H.; Wang, Y. Estimation of Moisture Content in Railway Subgrade by Ground Penetrating Radar. *Remote Sens.* **2020**, *12*, 2912. [CrossRef]
47. Alani, A.M.; Soldovieri, F.; Catapano, I.; Giannakis, I.; Gennarelli, G.; Lantini, L.; Ludeno, G.; Tosti, F. The Use of Ground Penetrating Radar and Microwave Tomography for the Detection of Decay and Cavities in Tree Trunks. *Remote Sens.* **2019**, *11*, 2073. [CrossRef]
48. Zeng, X.; McMechan, G.A. GPR characterization of buried tanks and pipes. *Geophysics* **1997**, *62*, 797–806. [CrossRef]
49. Kubiak, W.B. *Al Fustat: Its Foundation and Early Urban Development*; American University in Cairo Press: Cairo, Egypt, 1987.
50. Warren, C.; Giannopoulos, A.; Giannakis, I. gprMax: Open source software to simulate electromagnetic wave propagation for Ground Penetrating Radar. *Comput. Phys. Commun.* **2016**, *209*, 163–170. [CrossRef]

Disclaimer/Publisher's Note: The statements, opinions and data contained in all publications are solely those of the individual author(s) and contributor(s) and not of MDPI and/or the editor(s). MDPI and/or the editor(s) disclaim responsibility for any injury to people or property resulting from any ideas, methods, instructions or products referred to in the content.